# Experimental Study on ISAC Performance with Different Sensing Sequences

Diao Wang, Weiwei Chen, Yinghui He, Jianfeng Wang, Haiyan Luo, and Guanding Yu

***Abstract*—Integrated sensing and communication (ISAC) has been recognized as one of the key techniques for 6G, aiming at realizing smart sensing applications using wireless signals. However, existing investigations are limited to the algorithm design for smart sensing applications, and the parameters affecting sensing performance have not been thoroughly explored. To fill this gap, we study the impact of sensing sequences and communication parameters on the performance with real-world evaluations in this paper. Specifically, we develop a sensing platform based on USRP X310 and propose a novel packet detection algorithm as well as a time synchronization algorithm. Two typical applications, i.e., human pose recognition and dynamic gesture recognition, have been conducted under different sequences and communication parameters. The extensive results indicate that the sensing performance is identical across various sequences, and the relationship between the sensing performance and communication parameters is fully investigated.**

***Index Terms*—Wireless sensing, smart sensing application, sensing sequence, sensing performance, ISAC**

## I. Introduction

THE vision of 6G is to achieve ubiquitous intelligence [1], and integrated sensing and communication (ISAC) plays a crucial role as it endows networks with the ability to sense the real physical world. In contrast to conventional sensing relying on additional sensors, ISAC aims to reuse communication wireless signals, e.g., Wi-Fi and cellular signals, to sense the surrounding environment without extra cost [2]–[4].

The sensing applications can be divided into two categories: traditional sensing applications (e.g., model-based positioning and tracking) and smart sensing applications (e.g., learning-based activity recognition and fall detection) [5]. The former has been fully studied with the help of realistic simulation systems [6]. However, only few works focus on the latter since smart sensing applications require sensing data related to humans and conventional simulation systems are with limited real-world applicability. For example, the authors in [2] utilized Wi-Fi signals to realize the gesture recognition task and proposed a domain-independent feature body-coordinate velocity profile for improving the sensing performance, i.e., recognition accuracy. The authors in [3] employed LTE signals to achieve indoor respiration monitoring and designed a delicate signal processing scheme to mitigate interference caused by reflections from other moving objects. Existing work [7] utilized ultra-wideband signals to recognize the daily basic activity and proposed a CNN-LSTM model to achieve high classification accuracy. In previous studies, most of the attention has been paid to improving the sensing performance through signal processing, feature extraction, and deep learning network structure design. Nevertheless, existing works about sequence design only focused on traditional sensing applications. For example, the authors in [8] and [9] paid special attention to improving the traditional sensing performance, i.e., the peak to sidelobe ratio, detection rate, and false alarm rate, of different sensing sequences, e.g., m-sequence, gold sequence, and Zadoff-Chu (ZC) sequence. Meanwhile, in ISAC systems, sensing applications are realized with communication settings. Thus, communication parameters, such as bandwidth and subcarrier spacing, also impact the performance of sensing applications. For example, authors in [10] studied the impact of sampling rate and packet number on the accuracy of identifying whether a person is static or moving. However, comprehensive research on the influence of sequence and communication parameters on sensing performance remains insufficient.

Motivated by this, we aim to develop a real-world sensing platform and explore the impact of sensing sequences and communication parameters on the sensing performance. The main contributions of this work are summarized as follows.

- We are among the first ones to explore the influence of sensing sequences and communication parameters on the performance of sensing applications. Specifically, we consider three classical sequences: the cell-specific reference signals (CRS) sequence in LTE systems, the long training field (LTF) sequence in Wi-Fi systems, and the traditional sensing signal (TSS) used in radar systems. The investigated parameters include bandwidth, subcarrier spacing, number of receiving antennas, and sampling rate.
- We develop a sensing platform, composed of a sensing transmitter and a sensing receiver. In the receiver, we design a packet detection algorithm and a fine timing synchronization algorithm based on the correlation of channel state information (CSI) between two adjacent sensing sequences.
- We conduct a real-world test with two typical applications, i.e., human pose recognition and dynamic gesture recognition, using USRP X310. Extensive evaluations demonstrate that the sensing performance of different sensing sequences is similar and the sensing performance increases with the bandwidth and sampling rate but decreases with the subcarrier spacing.

The rest of this letter is organized as follows. Section II

Manuscript received April 30, 2024; revised August 04, 2024; accepted September 02, 2024. (*Diao Wang and Weiwei Chen contributed equally to this work.*) (*Corresponding author: Yinghui He.*)

D. Wang, W. Chen, Y. He, and G. Yu are with the College of Information Science and Electronic Engineering, Zhejiang University, Hangzhou 310027, China. e-mail: {diorwang, 22331145, 2014hyh, yuguanding}@zju.edu.cn.

J. Wang is with Lenovo Research, Lenovo Group Ltd., Beijing 100094, China. e-mail: wangjf20@lenovo.com.

H. Luo is with Lenovo (Shanghai) Information Technology Co., Ltd, Shanghai 201203, China. e-mail: luohy7@lenovo.com.

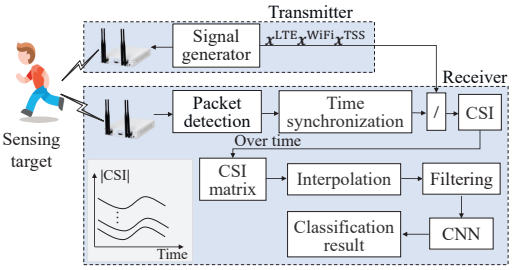


Fig. 1. Schematic diagram of the sensing platform.

introduces the sensing platform including a transmitter module and a receiver module. Section III presents the real-world test results and the letter is concluded in Section IV.

## II. Sensing Platform Design

The framework of the sensing platform contains two parts, i.e., a transmitter module and a receiver module, as illustrated in Fig. 1.[1] The former is utilized to transmit specific sensing signals and the latter is utilized for receiving the echo signals and obtaining the sensing results with the sensing algorithms.

### A. Sensing Transmitter

In the transmitter module, we consider an orthogonal frequency division multiplexing (OFDM) signal since it can be easily used in existing communication systems. In an OFDM system, the transmit sequence in the frequency domain, denoted by $\boldsymbol{s} \in \mathbb{C}^{N_r \times 1}$, undergoes the operations of zero-padding, inverse fast Fourier transform (IFFT), and CP insertion. Specifically, to mitigate intercarrier interference (ICI), a frequency-domain guard band by zero-padding is introduced, and the transmit sequence $\boldsymbol{s}$ are zero-padded as $\boldsymbol{B}^H\boldsymbol{s}$, where $\boldsymbol{B} = [\boldsymbol{0}_{N_r \times \frac{N_f - N_r}{2}}\ \boldsymbol{I}_{N_r}\ \boldsymbol{0}_{N_r \times \frac{N_f - N_r}{2}}]$ and $(\cdot)^H$ represents the Hermitian transpose of the matrix. Subsequently, to swiftly and effectively transform $\boldsymbol{s}$ from the frequency domain to the time domain, the IFFT operation is performed, as $\boldsymbol{F}^H\boldsymbol{B}^H\boldsymbol{s}$, where $\boldsymbol{F}$ is a shifted $N_f$-point discrete Fourier transform (DFT). Additionally, to reduce the impact of multipath effects on data, the last $N_c$ elements of the sequence are duplicated at the beginning of the sequence. Finally, the transmitted signal $\boldsymbol{x}$ in the time domain is denoted as

$$\boldsymbol{x} = \boldsymbol{A}\boldsymbol{F}^H\boldsymbol{B}^H\boldsymbol{s}, \tag{1}$$

where $\boldsymbol{A} \in \mathbb{C}^{N \times N_f}$ is the CP insertion matrix with $N = N_f + N_c$.

As we aim to evaluate the performance of different sequences in ISAC systems, we consider three classic sequences: the CRS sequence, the LTF sequence, and the TSS sequence. The first and second ones are used in two mainstream communication standards, i.e., LTE and Wi-Fi, respectively, offering fast and reliable wireless connectivity for devices, such as smartphones and tablets. The third one is a high-performance sensing sequence designed for traditional sensing applications, e.g., localization and tracking.

[1]We consider a strategic co-design scheme to achieve ISAC, and the pilot signals are used to facilitate sensing [11].

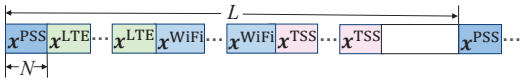


Fig. 2. The frame structure of the proposed sensing signal.

**CRS sequence**: The frequency-domain CRS sequence, denoted by $\boldsymbol{s}^{\mathrm{LTE}}$, can be expressed as

$$s^{\mathrm{LTE}}(n) = \frac{1}{\sqrt{2}}\left((1-2c(2n)) + i\,(1-2c(2n+1))\right), \tag{2}$$

where $c(n)$ is a pseudo-random sequence generated by a Gold sequence whose length is 31 [12]. The transmitted signal in the time domain is denoted by $\boldsymbol{x}^{\mathrm{LTE}}$.

**LTF sequence**: Wi-Fi standards comprise various versions, such as IEEE 802.11a/b/g/n/ac/ax, and each version has a different pilot sequence. To ensure backward compatibility, the modern Wi-Fi standard also contains the pilot used in the old version. Thus, to universally show the sensing performance of sequence in Wi-Fi systems, we consider the LTF sequence in IEEE 802.11a standard [13]. The frequency-domain LTF sequence is

$$\begin{aligned}\boldsymbol{s}^{\mathrm{WiFi}} = \{&1,1,-1,-1,1,1,-1,1,-1,1,1,1,1,1,1,\\ &-1,-1,1,1,-1,1,-1,1,1,1,1,1,0,1,-1,\\ &-1,1,1,-1,1,-1,1,-1,-1,-1,-1,\\ &-1,1,1,-1,-1,1,-1,1,-1,1,1,1,1\},\end{aligned} \tag{3}$$

corresponding to 53 subcarriers with the center one being the zero subcarrier. The transmitted signal in the time domain is denoted by $\boldsymbol{x}^{\mathrm{WiFi}}$.

**TSS sequence**: TSS sequence is used for detecting the potential target with the matched filtering. Thus, it is designed towards low autocorrelation by using WeCAN algorithm [14], Majorization–Minimization (MM) method [15], etc. In this paper, we adopt the WeCAN algorithm to generate the TSS sequence, denoted by $\boldsymbol{s}^{\mathrm{TSS}}$, and the length is set as $N_r$. The transmitted signal in the time domain is denoted by $\boldsymbol{x}^{\mathrm{TSS}}$.

To avoid the impact of environmental factors, such as Gaussian white noise, inconsistency of identical actions, or the variation of the environment, we repeat the three sequences mentioned above multiple times and then combine them together to construct the sensing signal, as shown in Fig. 2. It ensures that the differences in sensing performance are only caused by the differences in sensing sequence. Furthermore, to facilitate subsequent packet detection and time synchronization, we add the time-domain LTE primary synchronization sequence (PSS) [16], denoted by $\boldsymbol{x}^{\mathrm{PSS}}$, to the beginning of the sensing signal, and the length of $\boldsymbol{x}^{\mathrm{PSS}}$ is $N$. Moreover, the whole sensing signal needs to be continuously transmitted at a sampling rate and the interval between two successive transmitting signals is $L$.

### B. Sensing Receiver

In the receiver module, we first perform a packet detection algorithm to determine whether the sensing signal is received, which mainly utilizes the periodicity of the PSS sequence. Specifically, as shown in Fig. 3, the algorithm employs two sliding windows, denoted by W1 and W2, each with a length

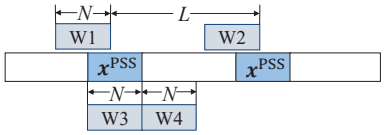


Fig. 3. Packet detection and coarse timing synchronization algorithms.

of $N$ and separated by a distance $L$, to calculate the correlation coefficient of the signals within two windows, as

$$\gamma(k) = \frac{\left|\sum_{n=0}^{N-1} y(k+n)^* y(k+L+n)\right|}{\sum_{n=0}^{N-1} |y(k+n)|\,|y(k+L+n)|}, \tag{4}$$

where $y(k)$ represents the received echo signal at the receiver with $k$ being the time index and $(\cdot)^*$ is the conjugate operation. When the correlation coefficient $\gamma(k)$ exceeds a threshold for a sequence of $M$ consecutive points, the sensing signal is detected.

The packet detection algorithm can only preliminarily determine the beginning index of the sensing sequences. To correctly measure the CSI, it is necessary to precisely obtain the beginning index of each sequence to avoid the symbol timing error. To this end, we adopt both coarse and fine timing synchronization methods. First, we use the energy detection algorithm of dual sliding windows [17] to perform coarse timing synchronization. As shown in Fig. 3, this algorithm utilizes two consecutive sliding windows, denoted by W3 and W4, each with a length of $N$, to calculate the signal energy within each window. Then, the ratio of the energy within the later window to that within the former window can be regarded as the decision variable, as

$$\beta(k) = \frac{\sum_{n=0}^{N-1} |y(k+n)|^2}{\sum_{n=0}^{N-1} |y(k-n-1)|^2}. \tag{5}$$

Upon the arrival of the $\boldsymbol{x}^{\mathrm{PSS}}$, $\beta(k)$ will reach its maximum value, indicating a noticeable peak, from which the coarse timing can be obtained.

Then, we perform fine timing synchronization after the coarse timing synchronization. Since the CSI does not have significant changes within a short time, the CSI measured from the received time-domain CRS sequence $\boldsymbol{y}^{\mathrm{LTE}}$, LTF sequence $\boldsymbol{y}^{\mathrm{WiFi}}$, and TSS sequence $\boldsymbol{y}^{\mathrm{TSS}}$ should be almost the same with the correct timing. To estimate the CSI from each sequence type, the CP of the sequence is first removed. Subsequently, to obtain the frequency-domain sequence, the fast Fourier transform (FFT) is performed. Then, the non-zero subcarriers are extracted. Finally, the CSI can be obtained by comparing the received signal to the transmitted one at the same subcarrier. Taking $\boldsymbol{y}^{\mathrm{LTE}}$ for example, the above process for estimating the CSI can be expressed as

$$\boldsymbol{h}^{\mathrm{LTE}} = \frac{\boldsymbol{BFQy}^{\mathrm{LTE}}}{\boldsymbol{s}^{\mathrm{LTE}}}, \tag{6}$$

where $\boldsymbol{Q}$ is the CP removal matrix. Similarly, we can also obtain the CSI of the LTF sequence $\boldsymbol{h}^{\mathrm{WiFi}}$ and the CSI of the TSS sequence $\boldsymbol{h}^{\mathrm{TSS}}$.

After obtaining the CSI, we can perform fine timing synchronization by assuming that the CSI keeps invariable within a short time. Fig. 4 depicts the variation of CSI's correlation between two adjacent sensing sequences. Taking $\boldsymbol{y}^{\mathrm{LTE}}$ for example, the $N$-length signal from the received signal does not precisely correspond to $\boldsymbol{x}^{\mathrm{LTF}}$ when there is timing offset, leading to the channel estimation error. Thus, the estimated CSI vectors over the frequency domain from different sequence types are different and the correlation between them is very low. As the absolute timing offset decreases, the estimation error decreases and thus the peak of the correlation is achieved when there is no timing offset.

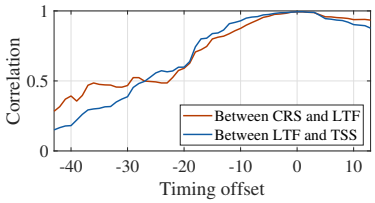


Fig. 4. The variation of CSI's correlation.

After the timing synchronization, precise CSI can be acquired. To facilitate subsequent classification tasks, we collect CSI samples over a period of time. Finally, we can obtain a CSI matrix, in which one dimension represents time and the other represents the subcarrier index. However, occurrences of packet loss would cause a non-uniform distribution of CSI information across the temporal dimension, which brings challenges for subsequent neural networks that require dimensional-consistent input. To tackle this problem, we employ a linear interpolation function to interpolate the CSI data along the temporal dimension.

Furthermore, to reduce the impact of noise on the final results, we employ a Butterworth lowpass filter to perform smoothing on the CSI data. Finally, we employ neural networks to separately train CSI matrices corresponding to the $\boldsymbol{x}^{\mathrm{LTE}}$, $\boldsymbol{x}^{\mathrm{WiFi}}$, and $\boldsymbol{x}^{\mathrm{TSS}}$ sequences, respectively.

## III. Evaluation

In this section, we first introduce the experiment settings and then conduct experiments to explore the sensing performance of the three sequences mentioned above.

### A. Implementation

To test the sensing performance of the three sequences, i.e., $\boldsymbol{x}^{\mathrm{LTE}}$, $\boldsymbol{x}^{\mathrm{WiFi}}$, and $\boldsymbol{x}^{\mathrm{TSS}}$, we establish an experimental platform using two USRP X310 devices, one for transmitting the sensing signal with one antenna and the other for receiving with two antennas. The experiment setup is shown in Fig. 5. The center frequency is set to 2.4GHz and the bandwidth is set to 20MHz. The default sensing sampling rate is 100Hz. The default subcarrier spacings for the CRS sequence, LTF sequence, and TSS sequence are 480kHz, 312.5kHz, and 480kHz, respectively. Two USRP devices are connected to the same external clock source to synchronize their RF frequencies, eliminating the need for carrier frequency offset compensation in the receiver [18]. The FFT number $N_f$ is set to 64 and the CP length $N_c$ is set to 14. Due to the different subcarrier spacing, the length of $\boldsymbol{s}^{\mathrm{LTE}}$, $\boldsymbol{s}^{\mathrm{WiFi}}$, and $\boldsymbol{s}^{\mathrm{TSS}}$ is set to 39, 53, and 39, respectively. Each sequence is repeated 6 times.

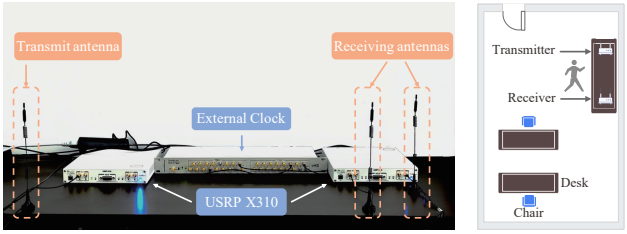


(a) USRP devices (b) Environment

Fig. 5. The experiment setup.

To enhance the credibility of the experimental results, we select two typical smart sensing applications in 6G scenarios: human pose recognition and dynamic gesture recognition [19]. The evaluation is conducted in an office, which is a widely used scenario for activity recognition applications. Four volunteers are invited to perform seven different behaviors in turn, i.e., sit, stand, walk, clap, push forward, left to right swap, and right to left swap. The first three behaviors and an additional "no volunteer" belong to the human pose recognition, and the last four behaviors belong to the dynamic gesture recognition. The classification accuracy is adopted as the metric to evaluate the sensing performance for both tasks. For each task, we collect 1,280 CSI samples as the dataset. Among them, 1,024 CSI samples are used for training, and 256 CSI samples are used for testing. We adopt a convolutional neural network (CNN) model with three convolution layers of $3 \times 3$ kernel size. It is trained and tested on a Linux server equipped with four NVIDIA GeForce GTX 3080 GPUs.

### B. Sensing Performance

**Overall sensing performance:** Fig. 6 shows the overall sensing performance under different numbers of receiving antennas, denoted by $N_{\mathrm{Rx}}$. The overall sensing performance of human pose recognition is higher than that of dynamic gesture recognition with $N_{\mathrm{Rx}} = 2$, since the hand is a smaller object with more complex articulations compared to the entire human body. Thus, the spatial resolution with two antennas cannot markedly improve the accuracy of the dynamic gesture recognition. Additionally, increasing $N_{\mathrm{Rx}}$ can significantly improve the sensing performance of human pose recognition tasks. This improvement is attributed to the higher spatial resolution associated with the increased number of receiving antennas. The variation of the relative spatial positions among various parts of human body is easier to be detected with a higher ability of spatial resolution. Therefore, an increase in the number of receiving antennas leads to a notable improvement in the sensing performance of human pose recognition tasks. However, increasing the number of receiving antennas (from one to two) has little impact on dynamic gesture recognition tasks since the variation of the relative spatial positions among fingers is relatively small.

**Effect of the bandwidth:** Fig. 7 shows the effect of bandwidth on the sensing performance. Sensing performance increases for both tasks as the bandwidth becomes wider. This is because a wider bandwidth means more information for sensing, which improves classification accuracy. However, when the bandwidth reaches around 11 MHz, the sensing performance remains relatively constant despite further increases. This is because the data collected at this bandwidth already contains sufficient valid information, and further increasing the bandwidth does not significantly improve the sensing performance. Additionally, 11 MHz can be defined as the saturation bandwidth for the sensing performance. Knowing the saturation point of sensing performance can avoid excessive resource allocation for performance improvement. Furthermore, the sensing performance among different sequences is almost the same since the CSI estimated from different sequences remains almost the same.

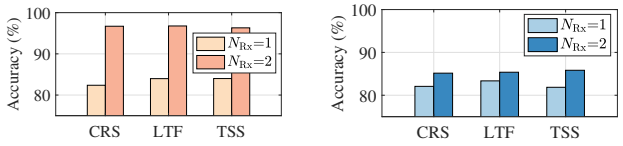


(a) Human pose recognition (b) Dynamic gesture recognition

Fig. 6. Overall sensing performance versus sensing sequences.

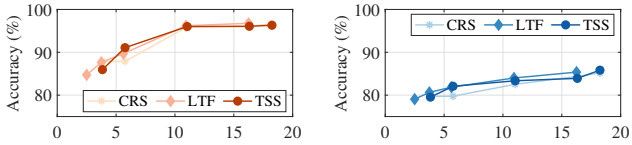


(a) Human pose recognition (b) Dynamic gesture recognition

Fig. 7. Sensing performance versus bandwidth in MHz.

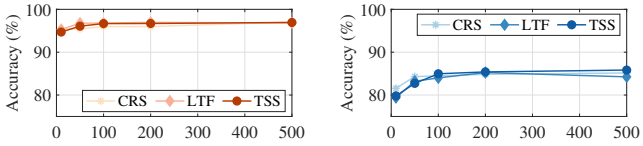


(a) Human pose recognition (b) Dynamic gesture recognition

Fig. 8. Sensing performance versus sampling rate in Hz.

**Effect of the sampling rate:** Fig. 8 shows the sensing performance under different sampling rates. Since human pose keeps stationary, different sensing sampling rates do not significantly affect the sensing performance of human pose recognition tasks, as shown in Fig. 8(a). For dynamic gesture recognition tasks, the sensing performance increases with the increasing sensing sampling rate and remains relatively constant after 200 Hz. Therefore, 200 Hz can be defined as the saturation sensing sampling rate for dynamic gesture recognition tasks. This is reasonable since the frequency of dynamic gestures is typically less than 200 Hz. Furthermore, the sensing performance of different sequences also exhibits minimal differences due to the same reason mentioned above.

**Effect of the subcarrier spacing:** Fig. 9 shows the effect of subcarrier spacing on the sensing performance. Under a constant bandwidth, we can vary the number of subcarriers to control the subcarrier spacing. We can observe that the sensing performance decreases with the subcarrier spacing. This is because different subcarriers carry different information and more information can be obtained as the subcarrier spacing becomes narrow, leading to a better sensing performance. Additionally, when the subcarrier spacing is small, the carried information contained in adjacent subcarriers is similar, leading to the low impact of the subcarrier spacing on the accuracy. Specifically, it is evident from the figure that when the subcarrier spacing is less than 3 MHz, there is minimal variation in sensing performance for both human pose recognition and

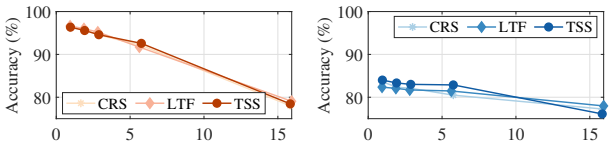


(a) Human pose recognition (b) Dynamic gesture recognition

Fig. 9. Sensing performance versus subcarrier spacing in MHz.

dynamic gesture recognition. These results suggest that this subcarrier spacing is sufficient to support both tasks. Thus, 3 MHz can be recognized as the saturation subcarrier spacing for two applications. Further reducing the subcarrier spacing is not cost-effective since it increases the number of subcarriers, adding a burden to the neural network's training process while offering marginal improvements in sensing performance.

Based on the above results, for the studied two applications, it is suggested to use the existing communication sequences, i.e., CRS and LTF, and the bandwidth and subcarrier spacing could be set as 11 MHz and 3 MHz, respectively. The sampling rate could be set as 100 Hz for the human pose recognition but 200 Hz for the dynamic gesture recognition. Additional resources only provide marginal gains in sensing performance.

### C. Communication Performance

Since the wireless channel model has been developed for decades and widely verified to be close to the real-world channel, we adopt the simulation method to test the communication performance. The cluster delay line model used in the 3GPP standard [20] is adopted. We adopt 16 QAM modulation with the signal-to-noise ratio being 15 dB, and the sampling rate is set to 30.72 MHz. From Tab. I, we can find that the symbol error rate using the LTF sequence is the lowest when the subcarrier spacing is 480 kHz. When the subcarrier spacing is 980 kHz, the performance using the CRS or LTF sequence is higher than that using the TSS sequence. This result is reasonable since both CRS and LTF are specifically designed for communication systems but TSS is specifically designed for radar systems. Besides, the impact of bandwidth on communication performance is not consistent due to the diversified channel gain over the increased bandwidth.

TABLE I
THE SYMBOL ERROR RATE WITH DIFFERENT SEQUENCES

| Subcarrier spacing | Sequence | Bandwidth (MHz) | | | | |
|---|---|---|---|---|---|---|
| | | **3.84** | **5.76** | **11.52** | **16.32** | **18.24** |
| 480 kHz | CRS | 7.31 % | 8.57 % | 6.48 % | 7.54 % | 6.63 % |
| | LTF | **5.65 %** | **5.71 %** | **6.43 %** | **5.99 %** | **5.37 %** |
| | TSS | 8.31 % | 8.20 % | 6.99 % | 8.83 % | 7.34 % |
| 960 kHz | CRS | **6.31 %** | 6.78 % | **7.17 %** | 7.48% | 7.22 % |
| | LTF | 6.98 % | **6.77 %** | 7.34 % | **6.57 %** | **5.93 %** |
| | TSS | 10.38 % | 8.66 % | 8.38 % | 8.15 % | 8.75 % |

## IV. Conclusion

In this paper, we have developed a sensing platform for exploring the impact of sensing sequences and communication parameters on various sensing applications. Specifically, with three classical sequences, i.e., CRS, LTF, and TSS, we have conducted extensive experiments on human posture recognition and gesture recognition using the USRP X310. The results demonstrate that the sensing performance among different sequences is almost the same. Additionally, the sensing performance increases with the bandwidth and sampling rate but decreases with the subcarrier spacing. Notably, the saturation bandwidth, sampling rate, and subcarrier spacing of sensing performance identified in the experiments are of significant importance for the implementation of sensing applications.

## References


[1] M. Latva-aho and K. Leppänen, "Key drivers and research challenges for 6G ubiquitous wireless intelligence," 6G Flagship, Univ. Oulu, Oulu, Finland, Sep. 2019.

[2] Y. Zhang et al., "Widar3.0: Zero-effort cross-domain gesture recognition with Wi-Fi," *IEEE Trans. Pattern Anal. Mach. Intell.*, vol. 44, no. 11, pp. 8671–8688, Nov. 2022.

[3] Y. Feng, Y. Xie, D. Ganesan, and J. Xiong, "LTE-based pervasive sensing across indoor and outdoor," in *Proc. ACM SenSys*, Nov. 2021, pp. 138–151.

[4] D. Wen, P. Liu, G. Zhu, Y. Shi, J. Xu, and S. Cui, "Task-oriented sensing, computation, and communication integration for edge AI inference with multiple devices," *IEEE Trans. Wireless Commun.*, vol. 23, no. 3, pp. 2486–2502, Mar. 2024.

[5] S. Sony, S. Laventure, A. Sadhu, "A literature review of next-generation smart sensing technology" *Struct. Control Health Monit.*, vol. 26, no. 3, pp. e2321, Jan. 2019.

[6] C. Gentner, T. Jost, W. Wang, S. Zhang, A. Dammann and U. -C. Fiebig,"Multipath assisted positioning with simultaneous localization and mapping" *IEEE Trans. on Wireless Commun.*, vol. 15, no. 9, pp. 6104–6117, Sep. 2016.

[7] J. Maitre, K. Bouchard, C. Bertuglia, and S. Gaboury, "Recognizing activities of daily living from UWB radars and deep learning," *Expert Syst. Appl.*, vol. 164, Feb. 2021, Art. no. 113994.

[8] C. Sturm and W. Wiesbeck, "Waveform design and signal processing aspects for fusion of wireless communications and radar sensing," *Proc. IEEE*, vol. 99, no. 7, pp. 1236–1259, Jul. 2011.

[9] F. Zhang, T. Mao, and Z. Wang, "Doppler-resilient design of CAZAC sequences for mmWave/THz sensing applications," *IEEE Trans. Veh. Technol.*, vol. 73, no. 2, pp. 2878–2883, Feb. 2024.

[10] C. Wu, Z. Yang, Z. Zhou, X. Liu, Y. Liu, and J. Cao, "Non-invasive detection of moving and stationary human with WiFi," *IEEE J. Sel. Areas Commun.*, vol. 33, no. 11, pp. 2329–2342, Nov. 2015.

[11] Z. Wei et al., "Integrated sensing and communication signals toward 5G-A and 6G: A survey," *IEEE Internet of Things Journal*, vol. 10, no. 13, pp. 11068—11092, Jan. 2023.

[12] *LTE; Evolved Universal Terrestrial Radio Access (E0UTRA); Physical Channels and Modulation (3GPP TS 36.211 Version 15.6.00 Release 15)*, document TS 36 211 V15.6.0, 3GPP, Jul. 2019.

[13] *IEEE Standard for Information Technology-Telecommunications and Information Exchange Between Systems Local and Metropolitan Area Networks-Specific Requirements—Part 11: Wireless LAN Medium Access Control (MAC) and Physical Layer (PHY) Specifications*, IEEE Standard 802.11-2016 (Revision IEEE Std 802.11-2012), pp. 1–3534, Dec. 2016.

[14] P. Stoica, H. He, and J. Li, "New algorithms for designing unimodular sequences with good correlation properties," *IEEE Trans. Signal Process.*, vol. 57, no. 4, pp. 1415–1425, Apr. 2009.

[15] L. Zhao, J. Song, P. Babu, and D. P. Palomar, "A unified framework for low autocorrelation sequence design via majorization–minimization," *IEEE Trans. Signal Proces.*, vol. 65, no. 2, pp. 438–453, Jan. 2017.

[16] J.-I. Kim, J.-S. Han, H.-J. Roh, and H.-J. Choi, "SSS detection method for initial cell search in 3GPP LTE FDD/TDD dual mode receiver," in *Proc. ISCIT*, Sep. 2009, pp. 199–203.

[17] J. Terry and J. Heiskala, *OFDM Wireless LANs: A Theoretical and Practical Guide.* Indianapolis, IN, USA: Sams, 2002.

[18] K. Alemdar, D. Varshney, S. Mohanti, U. Muncuk, and K. Chowdhury, "RFClock: Timing, phase and frequency synchronization for distributed wireless networks," in *Proc. ACM MobiCom*, Sep. 2021, pp. 15–27.

[19] D. K. P. Tan et al., "Integrated sensing and communication in 6G: Motivations, use cases, requirements, challenges and future directions," in *Proc. IEEE JC&S*, Feb. 2021, pp. 1–6.

[20] 3rd Generation Partnership Project (3GPP) Radio Access Network Working Group, "Study on channel model for frequencies from 0.5 to 100 GHz," (release 15) (Vol. 15), 3GPP, Sophia Antipolis, France, Tech. Rep. 38.901, 2018.